

Distinct pressure evolution of coupled nematic and magnetic order in FeSe

Anna E. Böhrer,^{1,2,*} Karunakar Kothapalli,^{1,3,4,*} Wageesha T. Jayasekara,^{1,3} John M. Wilde,^{1,3} Bing Li,^{1,3} Aashish Sapkota,^{1,3} Benjamin G Ueland,^{1,3} Pinaki Das,^{1,3} Yumin Xiao,⁵ Wenli Bi,^{6,7} Jiyong Zhao,⁶ E. Ercan Alp,⁶ Sergey L. Bud'ko,^{1,3} Paul C. Canfield,^{1,3} Alan I. Goldman,^{1,3} and Andreas Kreyssig^{1,3}

¹Ames Laboratory, U.S. DOE, Iowa State University, Ames, Iowa 50011, USA

²Institut für Festkörperphysik, Karlsruhe Institute of Technology, 76021 Karlsruhe, Germany

³Department of Physics and Astronomy, Iowa State University, Ames, Iowa 50011, USA

⁴College of Arts and Sciences, King University, Bristol, Tennessee, 37620, USA

⁵HPCAT, Geophysical Laboratory, Carnegie Institution of Washington, Argonne, IL 60439, USA

⁶Advanced Photon Source, Argonne National Laboratory, Argonne, Illinois 60439, USA

⁷Department of Geology, University of Illinois at Urbana-Champaign, Urbana, Illinois 61801, USA

FeSe, despite being the structurally simplest compound in the family of iron-based superconductors, shows an astoundingly rich interplay of physical phenomena including nematicity and pressure-induced magnetism. Here, we present a microscopic study of these two phenomena by high-energy x-ray diffraction and time-domain Mössbauer spectroscopy on FeSe single crystals over a wide temperature and pressure range. The topology of the pressure-temperature phase diagram is a surprisingly close parallel to the well-known doping-temperature phase diagram of BaFe₂As₂ generated through partial Fe/Co and Ba/Na substitution. In FeSe with pressure p as a control parameter, the magneto-structural ground state can be tuned from "pure" nematic — paramagnetic with an orthorhombic lattice distortion — through a strongly coupled magnetically ordered and orthorhombic state to a magnetically ordered state without an orthorhombic lattice distortion. The magnetic hyperfine field increases monotonically over a wide pressure range. However, the orthorhombic distortion initially decreases under increasing pressure, but is stabilized by cooperative coupling to the pressure-induced magnetic order. Close to the reported maximum of the superconducting critical temperature T_c (occurring at $p = 6.8$ GPa), the orthorhombic distortion suddenly disappears and FeSe remains tetragonal down to the lowest temperature measured. Analysis of the structural and magnetic order parameters suggests an independent origin of the structural and magnetic ordering phenomena, and their cooperative coupling leads to the similarity with the canonical phase diagram of iron pnictides.

I. INTRODUCTION

A fascinating characteristic of iron-based superconductors is their complex phase diagrams, and a decade of research has revealed intricate relationships between their magnetism, structure and superconductivity. Most parent compounds of the iron-based superconductors support an antiferromagnetic ground state, and, similar to many other unconventional superconductors, the antiferromagnetic order needs to be sufficiently suppressed for superconductivity to occur. The antiferromagnetic order in the iron-based compounds is typically stripe-type, characterized by a wavevector that breaks the tetragonal lattice symmetry¹. Hence, when stripe-type magnetic order forms, the lattice necessarily distorts from its high-temperature tetragonal structure and becomes orthorhombic². A dome of superconductivity arises around the point at which the magnetic order and lattice distortion are suppressed by a tuning parameter like doping or pressure, and the fluctuations related to the suppressed magnetic order and lattice distortion are a promising candidate for the superconducting pairing glue. Even seemingly special cases like the 10-3-8 material Ca₁₀(Pt₃As₈)(Fe₂As₂)₅ with a more complex chemical structure and disorder essentially fit into this picture³.

There are two intriguing exceptions to the intimate relationship between the orthorhombic distortion and

stripe-type magnetism, both of which have separately generated enormous interest. First, it was observed soon after the discovery of superconductivity in Fe-based materials that the orthorhombic lattice distortion may decouple from the stripe-type magnetic order and occur at a higher temperature ($T_s > T_N$)⁴⁻⁶. This has sparked the idea that the structural distortion is related to an independent "nematic" degree of freedom⁷ that could, in principle, exist without the magnetic order. Nevertheless, the orthorhombic distortion has theoretically been shown to be a likely consequence of stripe-type magnetic fluctuations⁷⁻⁹. Such split transitions are indeed very common and observed in pure and underdoped 1111-type materials⁴, in transition-metal substituted BaFe₂As₂¹⁰ and SrFe₂As₂, and in Co-substituted NaFeAs¹¹.

A few years later, it was discovered that magnetic order in certain iron-based systems can, in fact, also occur without an orthorhombic lattice distortion¹²⁻¹⁴. These intriguing "C4-type", tetragonal magnetic phases were shown to arise from a coherent superposition of the two symmetry-equivalent, stripe-type antiferromagnetic wavevectors¹⁵. The occurrence of magnetic order within a tetragonal structure is almost ubiquitous to hole-doped 122-type systems, occurring in Ba(Fe,Mn)₂As₂¹⁶, (Ba,K)Fe₂As₂^{12,14,17,18}, (Ba,Na)Fe₂As₂^{13,19}, (Sr,Na)Fe₂As₂^{15,20} and (Ca,Na)Fe₂As₂²¹, and was recently also shown in effectively hole-doped CaK(Fe,Ni)₄As₄²².

FeSe has generated enormous interest over the past few years as an extreme case of nematicity^{23–32}. At ambient pressure, FeSe exhibits a tetragonal-to-orthorhombic transition close to $T_s = 90$ K and no magnetic order down to sub-Kelvin temperatures³³. In this sense, FeSe is the iron-based material with the largest extent of a purely nematic phase. FeSe exhibits a complex magnetic fluctuation spectrum with intensity occurring around both the stripe-type and Néel-type wavevectors²⁵, and the spectral weights shift in favor of the stripe-type fluctuations below $T_s = 90$ K³⁴. A second reason why FeSe has generated excitement is the high tunability of its superconducting transition temperature T_c . Whereas ambient-pressure FeSe is superconducting below a modest T_c of ~ 8 K³⁵, T_c quadruples to 37 K under hydrostatic pressure^{36–39}. Studies of monolayer films of FeSe grown on SrTiO₃ have even shown evidence for $T_c > 100$ K (Ref. 40).

The temperature-pressure phase diagram of FeSe has been uncovered only incrementally. The structural transition is suppressed under pressure^{43–46}, pressure-induced magnetic order was demonstrated for $p > 0.8$ GPa and T_N increases with further increasing pressure^{33,42,44,45,47}. This, at first glance, represents a clear difference between FeSe and "typical" iron arsenides⁴⁸. Under pressure, the structural and magnetic phase lines for FeSe in fact merge into a concomitant magneto-structural transition⁴⁵, indicating that the magnetic ground state is orthorhombic and presumably the same stripe-type as occurs in other iron-based materials. The occurrence of stripe-type magnetic order is also suggested by NMR and μ SR results^{46,49}. The magneto-structural transition temperature traces out a dome with increasing pressure, with a maximum of 45 K occurring around 5 GPa⁴².

Here, we present a microscopic study of the magnetism, crystallographic symmetry, and in-plane lattice parameters of FeSe under hydrostatic pressure. The temperature dependence of the ordered magnetic hyperfine field and of the orthorhombic distortion in vapor-grown single crystals have been determined over a pressure range of $p = 0$ –10 GPa using high-energy x-ray diffraction and nuclear forward scattering. Figure 1 summarizes the experimental results. In the temperature-pressure phase diagram of FeSe in Fig. 1(a), the nematic, tetragonal-paramagnetic (T+PM) region on the low-pressure side borders an orthorhombic-magnetically-ordered dome (OR+M). We find that magnetic order persists on the high-pressure side of the magnetic dome in the absence of an orthorhombic distortion (T+M). The whole phase diagram is "cut-off" by a sharp and first-order structural transition at $p = 7.7$ GPa into an orthorhombic "OR2" phase^{50,51}. The low-temperature values of the magnetic and structural order parameters are shown in Fig. 1(b). The ordered magnetic hyperfine field increases monotonically over the orthorhombic-magnetic dome, whereas the orthorhombic distortion has a complex pressure dependence and mainly decreases on increasing pressure. The temperature-pressure phase diagram of FeSe is a surprisingly close parallel to the temperature-doping phase

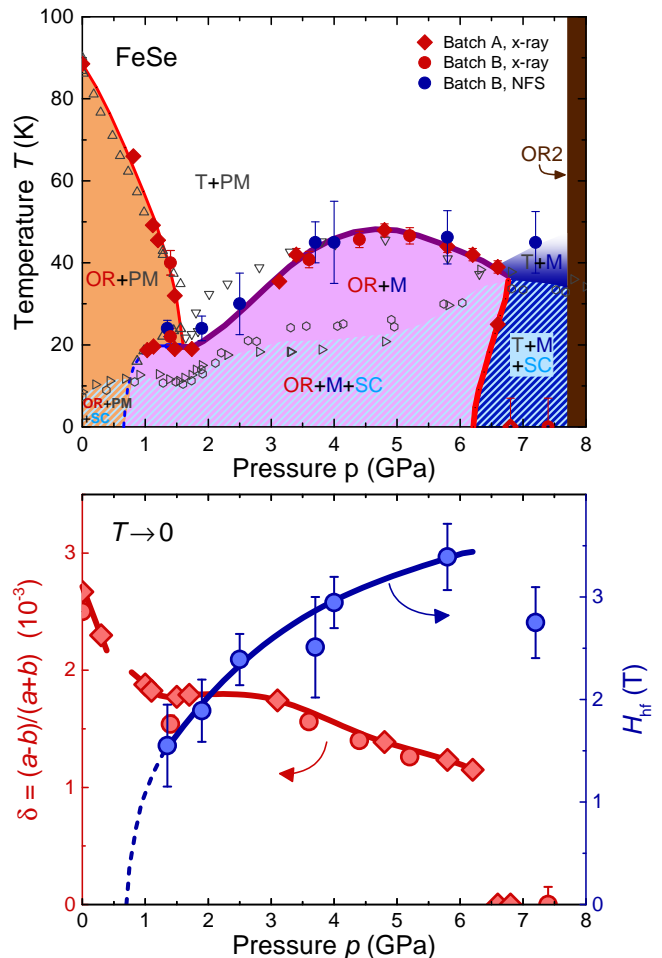


FIG. 1. (a) Temperature-pressure phase diagram of bulk FeSe. The structural transition temperatures were obtained by x-ray diffraction measurements on two different batches: A (red circles) and B (red diamonds). T (OR) stands for the tetragonal (orthorhombic) phase and OR2 stands for the reduced-volume high-pressure orthorhombic phase. SC denotes the superconducting state. PM (M) indicates paramagnetic (magnetically ordered) regions of the phase diagram as determined from nuclear-forward-scattering experiments on samples from batch B, with the transition temperature indicated by blue circles. Thick (thin) lines represent first (second) order phase transitions, respectively. Data from other reports are shown by open gray symbols for comparison and completeness: up triangles⁴¹ and down triangles⁴² indicate the structural and magnetostructural transitions, right triangles⁴² and hexagons⁴³ indicate the superconducting transition. (b) Pressure-dependence of the zero-temperature limit of the orthorhombic distortion, i.e. the structural order parameter (left axis), and the ordered hyperfine field (right axis), as a proxy for the magnetic order parameter.

diagram of the 122-type systems, if both electron-and hole-doping are considered. On the other hand, an analysis of the pressure dependent orthorhombic distortion and magnetic hyperfine field suggests that these ordering phenomena have distinct origins, although the order

parameters couple cooperatively.

II. EXPERIMENTAL METHODS

Single-crystals of FeSe were prepared by chemical vapor transport as described in Ref. 52. Batch A samples are from several batches using natural-abundance elements, whereas batch B samples are from a batch prepared using 95% enriched ^{57}Fe . As described in Ref. 52, the sample properties can vary even with tiny variations in growth conditions. Batch B was found to have less perfect mosaicity and less sharp phase transitions than samples from batch A, however batch A and B both have very similar transition temperatures and values for the orthorhombic distortion (see Fig. 1).

High-energy (100 keV), high-resolution x-ray diffraction experiments were performed at endstation 6ID-D of the APS Argonne on samples from batches A and B. The samples were pressurized in diamond anvil cells (DACs) using He gas as a highly hydrostatic pressure-transmitting medium. We used diamonds with 600 μm culets and stainless-steel and CuBe gaskets preindented to thicknesses of $\sim 60 \mu\text{m}$ and with laser-drilled holes of $\sim 250 - 350 \mu\text{m}$. The position of a fluorescence line for ruby was used for ambient-temperature pressure calibration. Measurements of the lattice parameter of polycrystalline silver were used for in-situ pressure determination at all temperatures, so that the actual temperature-dependent pressure values are reported. Extended regions of selected reciprocal lattice planes and the powder diffraction pattern of silver were recorded by a MAR345 image plate system positioned 1.474 m behind the DAC, as the DAC was rocked by up to $\pm 3.2^\circ$ about two independent axes perpendicular to the incident x-ray beam. High-resolution diffraction patterns of selected Bragg reflections of samples from batch A were also recorded using a Pixirad-1 detector positioned 1.397 m behind the DAC while rocking around one of the two axes perpendicular to the x-ray beam. The in-plane lattice parameters were determined by fitting the Bragg peak positions after integrating the data over the transverse scattering directions. This procedure was used for both the data recorded by the Pixirad-1 detector and by the MAR345 image plate system.

Nuclear forward scattering (NFS), i.e. time-domain Mössbauer spectroscopy, was performed on stations 3ID-B and 16ID-D at the APS on samples from batch B. Diamond anvil cells with He as a pressure transmitting medium and ruby as an in-situ pressure calibrant were used and the pressure cells were set up in a similar way as for the diffraction experiments. At 3ID-B, miniature panoramic DACs⁵³ were used. The incident x-ray beam was monochromated to the ^{57}Fe nuclear resonance energy of 14.4125 keV with a resolution of 2 meV and the intensity of the scattered beam in the forward direction was recorded by an Avalanche Photo Diode detector. The beam size at 3ID-B and 16ID-D was $10 \times 10 \mu\text{m}^2$ and

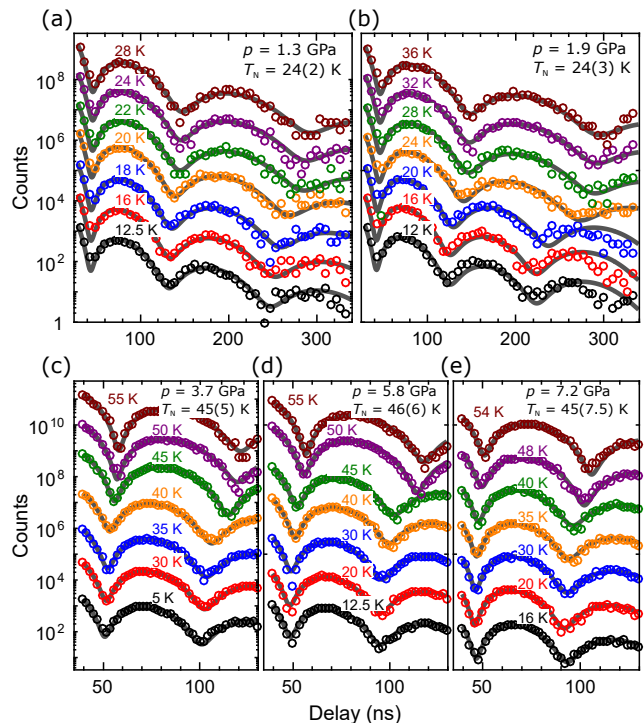


FIG. 2. ^{57}Fe nuclear-forward-scattering spectra for FeSe at selected pressures and temperatures. Data are offset for clarity, and dark gray lines show fits to the data using CONUSS. Data in (a) and (b) were collected on a 6 μm thick sample from batch B in the long-pulse mode with a 1.5 μs clear time for measurements. Data in (c)–(e) were collected on an 18 μm thick sample from batch B using the 24 bunch standard timing mode of the APS, with a 153 ns separation between x-ray pulses.

$20 \times 30 \mu\text{m}^2$, respectively. Spectra for $p \geq 2.5$ GPa were collected at 16ID-D using the 24-bunch standard timing mode of the Advanced Photon Source, where an x-ray pulse of 80 ps duration hits the sample with a periodicity of 153 ns. Spectra for $p < 2.5$ GPa were collected at 3ID-B beamline in the so-called hybrid mode with a 1.5 μs clear time for measurements after the initial excitation pulse hits the nuclei. This long-pulse mode reduces the counting rate by an order of magnitude. However, it drastically improves the sensitivity and precision of determining the internal magnetic hyperfine field due to the increased observation time of the nuclear decay, which is particularly relevant when hyperfine fields are very small. The program CONUSS⁵⁴ was used to analyze the spectra and determine the magnetic field hyperfine at the iron sites.

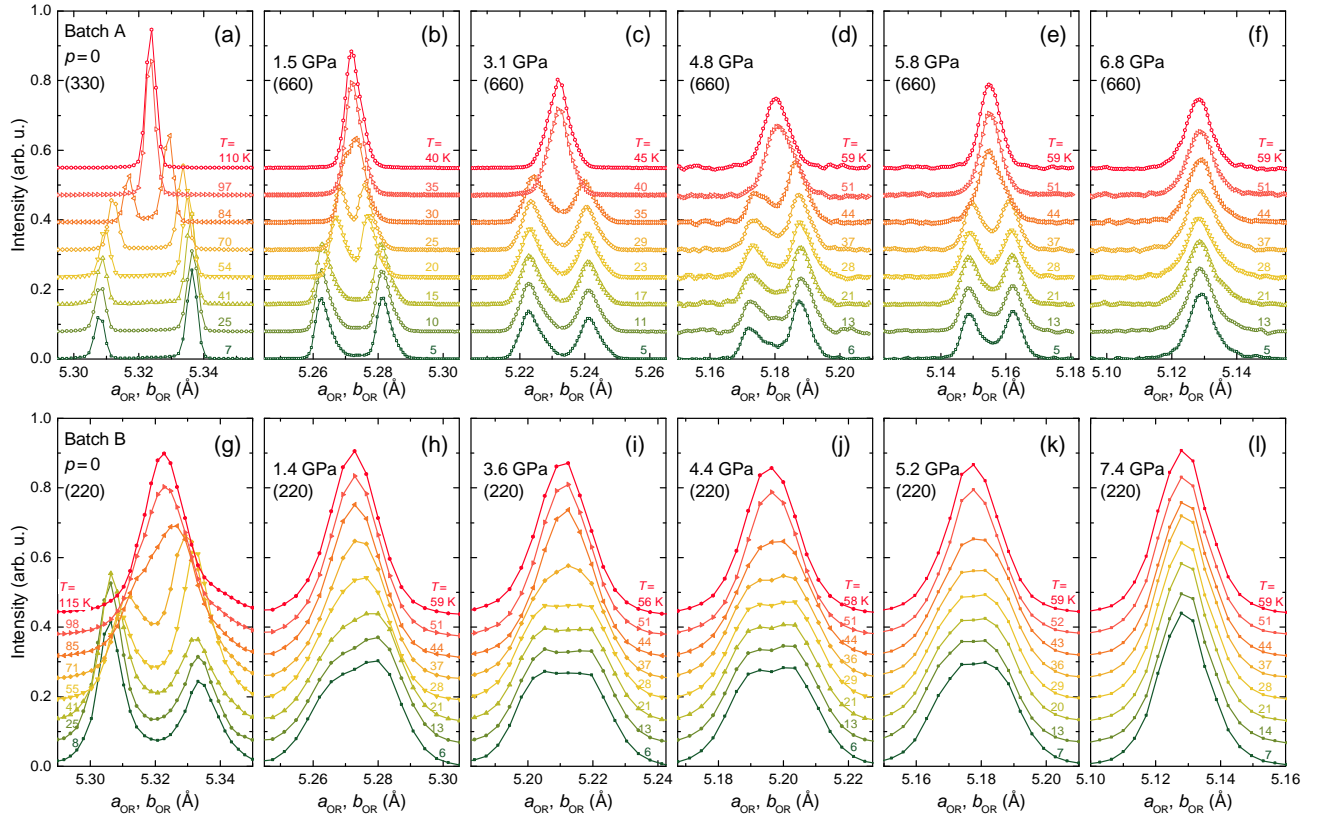


FIG. 3. High-energy x-ray diffraction patterns demonstrating the tetragonal to orthorhombic phase transition. a_{OR} and b_{OR} are the lattice parameters for the orthorhombic unit cell (a)-(f), X-ray intensity profiles taken across the (3 3 0) (a) and (6 6 0) [(b)-(f)] tetragonal unit cell Bragg peaks on samples from batch A for various pressures and temperatures. The peak splitting results from the orthorhombic distortion. (g)-(l), X-ray intensity profiles close to the (2 2 0) Bragg peaks for samples from batch B at various pressures and temperatures. Here, the peak splitting or broadening signals the orthorhombic distortion. The difference in peak profiles with respect to the upper panels results from the lower order of the chosen Bragg peak, the use of a different detector, and the broader mosaicity of samples from batch B.

III. RESULTS

A. Nuclear forward scattering and x-ray diffraction

Figure 2 shows the NFS spectra at various pressures up to 7.2 GPa, from which the information about the magnetic order is obtained. Data for low pressures were obtained to longer delay times on a 6 μm thick sample so that small magnetic hyperfine fields could be determined more accurately. Data for pressures above 2.5 GPa were obtained on an 18 μm thick sample. The observed quantum beats originate from a convolution of the hyperfine field, quadrupole splitting and sample thickness. A change in the spectra, most notably the shift of the minima, e.g., between 20 K and 24 K at 1.9 GPa, indicates that a magnetic phase transition has occurred. Such a transition is observed for pressures up to 7.2 GPa. At 1.3 GPa a similar, though more continuous shift is discernible and identified as a magnetic phase transition. The corresponding magnetic hyperfine fields are reported in Fig. 5 below.

Figures 3 and 4 show the results of high-energy x-ray

diffraction measurements made close to ($H H 0$)-type Bragg peaks and reveal the temperature and pressure dependence of the orthorhombic distortion. In Fig. 3 data on samples from batches A (obtained with the Pixirad-1 detector) and B (obtained with the MAR345 detector) are compared. An obvious difference in peak profiles results from the different orders of the chosen Bragg peaks, the use of different detectors, and the broader mosaicity of samples from batch B. A low-temperature peak-splitting or broadening indicates an orthorhombic ground state. Structural transitions are clearly visible for samples from both batches. At the highest pressures of 6.8 and 7.4 GPa, the absence of any peak splitting or broadening and the temperature independent peak profiles up to 60 K indicate a tetragonal ground state.

As already shown in Ref. 45, the ambient-pressure second-order tetragonal-to-orthorhombic transition at T_s is suppressed under pressure. At $p \gtrsim 1.5$ GPa, a first-order transition occurs at $T_N < T_s$ and the two transitions merge for slightly higher pressures. This first-order transition is observed in the same manner up to 5.8 GPa. To investigate the pressure-evolution of the orthorhom-

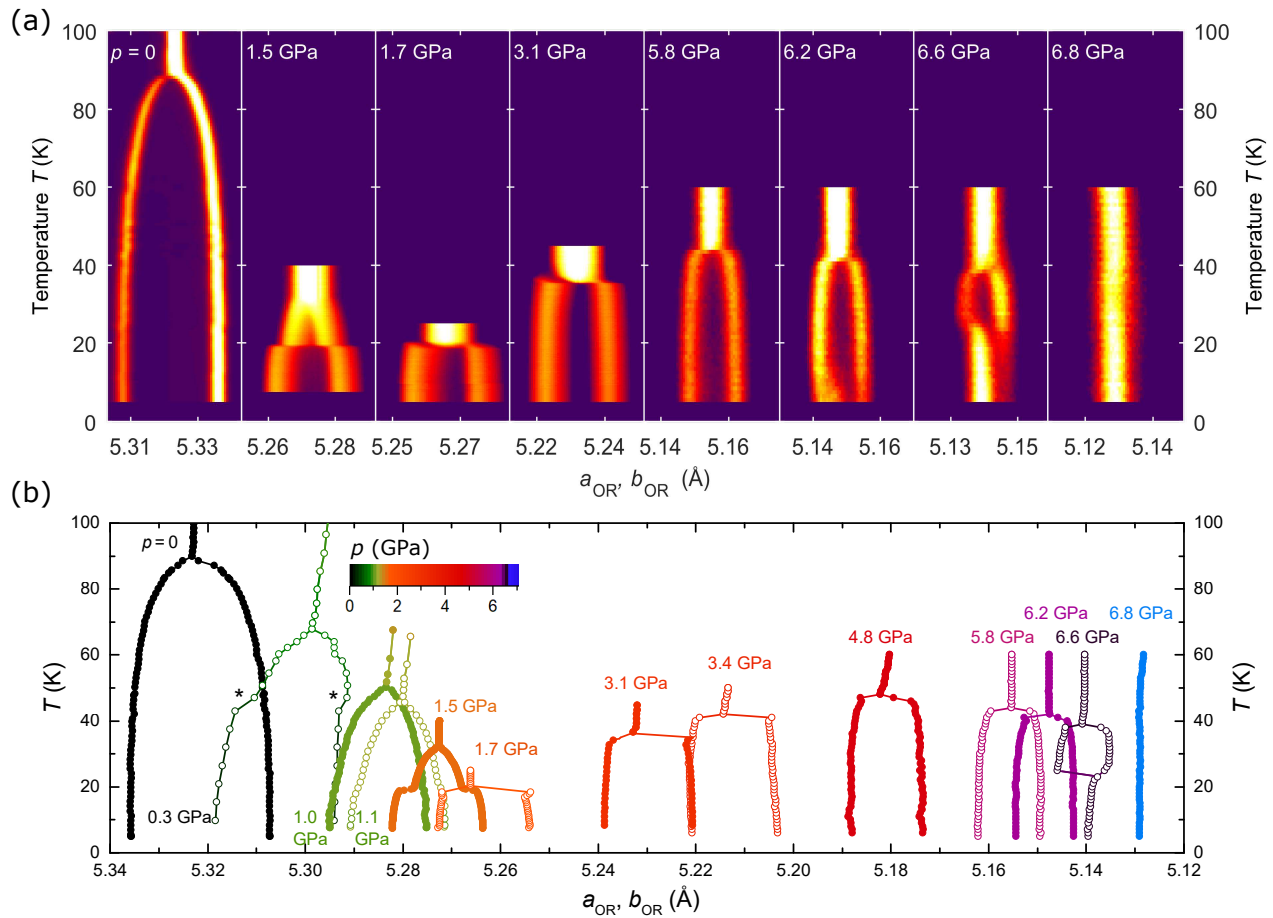


FIG. 4. Temperature dependence of the in-plane orthorhombic lattice parameters a_{OR} and b_{OR} of FeSe for various pressures. (a) The detector intensity for positions spanning the (3 3 0) or (6 6 0) tetragonal unit cell Bragg peaks integrated over the transverse scattering directions at various pressures. Low-pressure ($p \leq 3.1$ GPa) data are taken from Ref. 45. (b) Orthorhombic lattice parameters a_{OR} and b_{OR} as a function of temperature for various pressures. Stars mark the crossing of the He-solidification line, which entails a change in pressure (see color scale). Note that the horizontal scale decreases from left to right.

bic distortion of FeSe in more detail, samples from batch A have been studied with additional fine pressure steps between 5.8 and 6.8 GPa (Figure 4).

At pressures above 5.8 GPa, a new behavior is observed, which is most pronounced at $p = 6.6$ GPa. On decreasing temperature, the sample first undergoes the first-order tetragonal-to-orthorhombic transition, at $T_{s,N} = 39$ K, before it transforms back into a tetragonal structure at $T_r = 25$ K. At the just slightly higher pressure of 6.8 GPa, the sample remains tetragonal at all temperatures. We note that a small phase fraction ($\lesssim 15\%$) appears to become orthorhombic in a limited temperature range even at 6.8 GPa, apparently experiencing a slightly lower effective pressure due to small internal stresses. Similarly, at the lower pressure of 6.2 GPa, a tetragonal fraction of the sample ($\sim 20\%$) coexists with the major orthorhombic phase at base temperature. On heating, this phase fraction transforms to orthorhombic at $T_r \sim 12$ K. This "structurally reentrant" behavior is reminiscent of the "structural reentrance" in

hole-doped 122-type materials upon transition into the tetragonal magnetic phase^{13,15,21,55}.

Figure 4(b) shows the in-plane lattice parameters of the majority phase of FeSe vs. temperature for all the studied pressures. FeSe has a high compressibility and the tetragonal in-plane lattice parameter is decreased by 3.7% at 7 GPa. In the pressure range 1.7-4.8 GPa, the orthorhombic transition results in an asymmetric change of in-plane lattice parameters so that the average of the a and b lattice constants decreases at the transition, similar to the $\text{Ba}(\text{Fe},\text{Co})_2\text{As}_2$ system⁵⁶. This reverses at higher pressures, so that at ~ 6 GPa, the a - b average increases on cooling through T_s , similarly to underdoped $(\text{Ba},\text{K})\text{Fe}_2\text{As}_2$ ¹⁴.

B. Structural and magnetic order parameters

The temperature and pressure evolution of the orthorhombic order parameter $\delta = (a_{\text{OR}} - b_{\text{OR}})/(a_{\text{OR}} +$

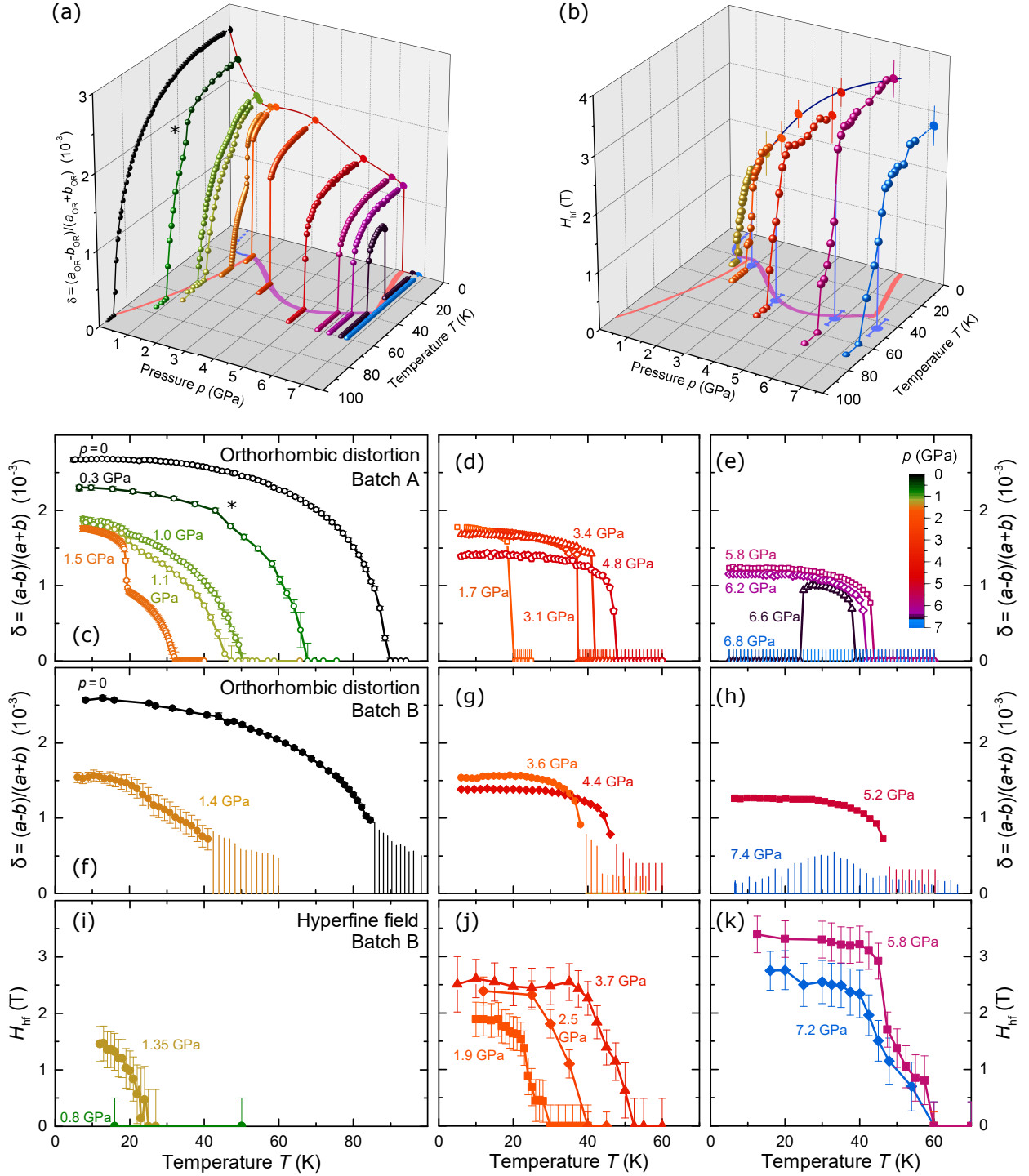


FIG. 5. Structural and magnetic order parameters of FeSe under pressure. (a), (b) Three-dimensional representation of the temperature- and pressure-dependence of the orthorhombic distortion, $\delta = (a_{\text{OR}} - b_{\text{OR}})/(a_{\text{OR}} + b_{\text{OR}})$, and magnetic hyperfine field, H_{hf} . Projections of the extrapolated low-temperature values are shown in the $T = 0$ plane. Lines are guides to the eye. The phase diagram from Fig. 1 is indicated in the basal, $T - p$ plane. (c)-(e) Orthorhombic distortion δ of samples from batch A as a function of temperature at various color coded pressures [see scale in (e)]. The star symbol marks the crossing of the He solidification line. (f)-(h) Orthorhombic distortions δ of samples from batch B. Vertical bars represent a possible inhomogeneous distortion above the midpoint of the structural transition deduced from peak broadening. (i)-(k) Hyperfine field H_{hf} at the Fe site for samples from batch B, determined from the fitting shown in Fig. 2. Data at 2.5 GPa from Ref. 45 are also reported. Error bars represent the estimated total uncertainty including systematic errors.

b_{OR}) and the magnetic hyperfine field H_{hf} at the iron site are presented in Fig. 5. Here, we also compare the diffraction results for the two different batches. The transitions are very sharp in samples from batch A, whereas samples from batch B exhibit clear tails to the transitions, which likely arise from inhomogeneities caused by internal stresses. The hyperfine fields deduced from the NFS spectra in Fig. 5(j,k) likely exhibit similar tails of the same origin. Nevertheless, transition temperatures can be well defined as the points of highest rate change of order parameters and the determined values of T_s agree well between the two batches (see Fig. 1).

A second-order structural transition occurs in the absence of magnetic order at the lowest pressures $p \lesssim 0.8$ GPa. At the slightly higher pressure of 1.35 GPa, magnetic order emerges in a second-order like transition at $T_N < T_s$. In an intermediate pressure range $\sim 1.7 - 6$ GPa, magnetic and structural transitions are both first order and are firmly coupled, as discussed in Ref. 45. The coupling between structural and magnetic order surprisingly breaks down at pressures $p \gtrsim 6.6$ GPa, when FeSe exhibits a tetragonal ground state even though an ordered magnetic hyperfine field is still observed at a pressure as high as 7.2 GPa. This indicates the presence of a tetragonal magnetic phase.

We note that the tetragonal magnetic state in $(\text{Sr,Na})\text{Fe}_2\text{As}_2$ was shown to be a coherent superposition of two spin-density waves and is characterized by two distinct Fe sites - one with zero and one with double the hyperfine field of the regular stripe-type phase¹⁵. Unfortunately, our time-domain Mössbauer spectroscopic experiment is unable to distinguish such a state from a state of the same hyperfine field on all Fe sites. Here, we show the results of fitting with a single hyperfine field, H_{hf} . A model in which zero moment is imposed for half of the Fe sites is able to fit our data at 7.2 GPa equally well, with a fitted value of $H_{\text{hf}} \approx 4.5$ T for the moment-bearing Fe-sites at base temperature. Nevertheless, it is also possible that FeSe exhibits a completely different type of magnetic order, as might be indicated by the presence of Néel type magnetic fluctuations at ambient pressure³⁴.

Figures 5(a)-(b) [see also Fig. 1(b)] summarize the temperature and pressure evolution of the structural and magnetic order parameters over the phase diagram. The low-temperature value of the magnetic hyperfine field of the orthorhombic-magnetic phase increases monotonically under pressure up to ~ 6 GPa, even though the magnetic transition temperature has a dome-like pressure dependence and peaks around 4.8 GPa. The orthorhombic distortion exhibits a complex temperature-pressure dependence. Initially, on increasing pressure, the value of the orthorhombic distortion is suppressed. The low-temperature value of δ barely changes as a function of pressure between 1 – 3.4 GPa and then gradually decreases under pressure over the range at which $T_{s,N}$ has a maximum. The structurally "reentrant" tetragonal behavior with vanishing lattice distortion at the lowest temperatures is limited over a very small pressure range

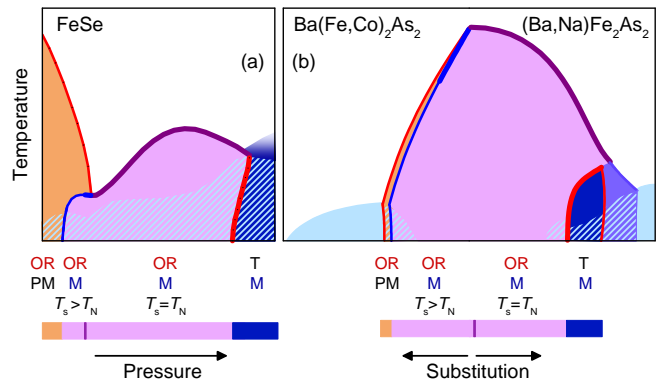


FIG. 6. Schematic phase diagrams of FeSe under pressure (this work) and BaFe_2As_2 doped with cobalt (Ref. 57) and sodium (Ref. 19). The phase lines and phases are color-coded as in Fig. 1. The evolution of magnetic/structural ground states from orthorhombic/paramagnetic (OR+PM), via orthorhombic/magnetically ordered (OR+M) with $T_s > T_N$, orthorhombic/magnetically ordered with $T_s = T_N$ to tetragonal/magnetically ordered (T+M) for increasing pressure in FeSe parallels the evolution of the ground states of BaFe_2As_2 from electron-doped to hole-doped.

$6.2 \lesssim p < 6.8$ GPa and the orthorhombic distortion is absent at all temperatures at 6.8 GPa.

IV. COMPARISON OF FeSe AND BaFe_2As_2 -BASED SUPERCONDUCTORS

The schematic temperature-pressure phase diagram of FeSe in Fig. 6(a) has remarkable similarities to the temperature-substitution phase diagram of the canonical BaFe_2As_2 iron-based superconductors [6(a)]. In particular, we consider substitution of Co on the Fe-site ("electron-doping") and substitution of Na on the Ba site ("hole-doping") as a way of tuning BaFe_2As_2 quasi-continuously as shown in Figure 6(b). Then, the sequence of magnetic/structural ground states and the topology of the phase diagrams formed by the corresponding phase lines are similar. FeSe at low pressures and slightly underdoped $\text{Ba}(\text{Fe,Co})_2\text{As}_2$ both have an orthorhombic paramagnetic ground state. On increasing pressure or decreasing Co content the ground state changes to orthorhombic and antiferromagnetic within a region for which $T_s > T_N$ until the structural and magnetic phase lines merge. On the high-pressure side of FeSe and in close to optimally doped $(\text{Ba,Na})\text{Fe}_2\text{As}_2$ a tetragonal magnetic ground state emerges.

A qualitative difference between FeSe under pressure and substituted BaFe_2As_2 becomes evident when the value of the orthorhombic and magnetic order parameters are considered. In the 122-type systems, the orthorhombic distortion, δ , and the ordered magnetic moment, M , in the low-temperature limit follow each other closely. Linear-quadratic coupling $\delta \propto M^2$ is theoretically expected^{2,8,61,62}. It has, for example, explicitly

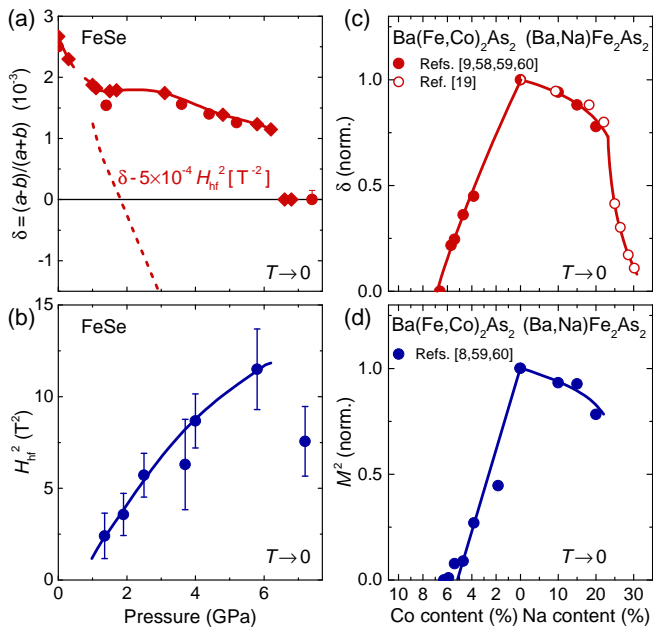


FIG. 7. Evolution of the orthorhombic and magnetic order parameters of FeSe and BaFe_2As_2 . (a) Low-temperature extrapolation of δ of FeSe as a function of pressure. The dashed line shows the experimental δ subtracted by a contribution proportional to H_{hf}^2 , which continues the trend of $\delta(p)$ from low pressures (in the absence of magnetic order). (b) Square of hyperfine field H_{hf}^2 of FeSe under pressure. (c) Low-temperature extrapolation of δ of $\text{Ba}(\text{Fe,Co})_2\text{As}_2$ (Refs. 9 and 58) and $(\text{Ba,Na})\text{Fe}_2\text{As}_2$ from Refs. 59 and 60 (full symbols) and 19 (open symbols). (d) Square of the ordered magnetic moment of $\text{Ba}(\text{Fe,Co})_2\text{As}_2$ ⁸ and $(\text{Ba,Na})\text{Fe}_2\text{As}_2$ ^{59,60}. Lines are a guide to the eye. The data from different references in (c),(d) are scaled at pure BaFe_2As_2 . Whereas the order parameters (approximately) obey linear-quadratic coupling $\delta \propto M^2$ in the 122-type system, this is not the case for FeSe.

been shown experimentally for $(\text{Ba,K})\text{Fe}_2\text{As}_2$ ⁵⁹, which features strongly coupled magneto-structural transitions. This proportionality does not hold for FeSe, where $H_{\text{hf}} \propto M$ increases monotonically up to ~ 7 GPa and δ has a complex non-monotonic pressure dependence (Figure 7).

One way to rationalize our results on FeSe is to assume that the material's tendency for an orthorhombic distortion at ambient pressure is independent of the pressure-induced magnetic order. Under increasing pressure, this structural instability is weakened and δ decreases, whereas the magnetic instability is strengthened. The low cost of orthorhombic distortion at moderate pressures likely favors a stripe-type antiferromagnetic order. By symmetry, an orthorhombic distortion and stripe-type magnetic order couple cooperatively so that the low-temperature value of δ should increase by an amount $\propto M^2$, whenever both types of order occur. If such a contribution to the experimental value of δ is subtracted, the initial trend of $\delta(p)$ indeed continues smoothly [dashed line in Fig. 7(b)]. Symmetry also dictates that structural and magnetic phase lines

merge when T_s meets T_N , because the stripe-type AFM state is necessarily orthorhombic. Only above ~ 6.6 GPa does any orthorhombic distortion become so unfavorable that tetragonal magnetic order is established instead of stripe-type antiferromagnetism. Thus, the origin of the orthorhombic distortion of FeSe at ambient pressure is likely independent from the pressure-induced magnetic order. Theoretically, the nematic order of FeSe at ambient pressure has been found to arise from a Pomeranchuk instability within a renormalization group analysis⁶³, which could explain the observed result. Similarly, the theoretically proposed antiferroquadrupolar order⁶⁴ is a candidate. The effect of pressure as a tuning parameter has been subject to numerous theoretical studies as well^{27,65–67}. Model⁶⁶ and ab-initio⁶⁷ calculations find a decrease of the tendency to charge order under pressure that could be associated with our results.

The similarity between FeSe under pressure and substituted BaFe_2As_2 does not hold for the pressure dependence of superconductivity. In Fig. 1 we report T_c as determined from zero resistance⁴² and the onset of diamagnetism⁴³. However, it has been questioned whether superconductivity can microscopically coexist with magnetic order in FeSe. The dc magnetization in Ref. 43 indicates an unchanged amount of diamagnetic shielding up to 7 GPa. Nevertheless, the superconducting transition becomes significantly broader in the pressure range in which orthorhombic magnetism and superconductivity overlap^{42,44} and the spin-lattice relaxation rate in NMR does not change at the putative T_c ⁴⁶, questioning bulk superconductivity. Similarly, such a coexistence has been questioned in $\text{Fe}(\text{Se,S})$ ⁶⁸. None of our diffraction or NFS results show any anomaly that could be associated with T_c . Since the question of bulk superconductivity in FeSe under pressure is not solved, any conclusion about relation between the tetragonal magnetic phase and superconductivity at high pressures has to be speculative. From the literature, it seems that T_c is maximized in this pressure range. We note that in hole-doped 122's, T_c tends to be slightly suppressed^{14,19} by the presence of the tetragonal magnetic phase.

V. CONCLUSION

In summary, we have studied the structural and magnetic phase diagram and order parameters of FeSe. We have exposed an unexpected variability of the pressure-induced magnetic order. It couples cooperatively with an orthorhombic distortion in the intermediate pressure range. However, at higher pressures, we have discovered the complete suppression of orthorhombic distortion and a tetragonal magnetic phase. This sets the stage for high-temperature superconductivity in FeSe under pressure. The topology of the temperature-pressure phase diagram of FeSe resembles closely the well-known phase diagram of electron/hole-doped BaFe_2As_2 . The origin of the nematic phase in BaFe_2As_2 -based materials is widely ac-

cepted to be tied to their stripe-type antiferromagnetism. Here, the pressure evolution of the magnetic and structural order parameters of FeSe leads us to suggest that the origin of the orthorhombic phase in FeSe is distinct from the pressure induced magnetic order. The cooperative coupling between orthorhombicity and magnetic order that is present in both FeSe and BaFe_2As_2 -based systems likely leads to the similarities in the phase diagrams.

VI. ACKNOWLEDGEMENTS

We would like to acknowledge the assistance of D. S. Robinson, C. Benson, S. Tkachev, S. G. Sinogeikin, Ross Hrubciak, Barbara Lavina, R. Somayazulu and M. Baldini, and helpful discussions with R. J. McQueeney. Work at the Ames Laboratory was supported by the Department of Energy, Basic Energy Sciences, Division of Materials Sciences & Engineering, under Contract No. DE-AC02-07CH11358. This research used resources of the Advanced Photon Source, a U.S. Department of Energy (DOE) Office of Science User Facility operated for the DOE Office of Science by Argonne National Laboratory under Contract No. DE-AC02-06CH11357. HPCAT operations are supported by DOE-NNSA under Award No. DE-NA0001974, with partial instrumentation funding by NSF. Use of the COMPRES-GSECARS gas loading system was supported by COMPRES under NSF Cooperative Agreement EAR 11-57758 and by GSECARS through NSF grant EAR-1128799 and DOE grant DE-FG02-94ER14466. Y.X. acknowledges the support of DOE-BES/DMSE under Award DE-FG02-99ER45775. W.B. acknowledges the partial support by COMPRES, the Consortium for Materials Properties Research in Earth Sciences under NSF Cooperative Agreement EAR 1606856.

Appendix A: High-pressure phase of FeSe

At just slightly higher pressures than those presented in Fig. 5 the samples of both batches undergo a severe structural transition illustrated in Fig. 8. This transition is well-known in literature^{37,38,50,51,69} and the high-pressure orthorhombic "OR2" phase has been identified as having MnP-type structure with a dramatic volume reduction of $\sim 10\%$ with respect to the layered PbO-type FeSe-phase that is stable at lower pressures. The inset in Fig. 8(a) shows sections of the $(HK0)$ scattering plane of the two phases at representative pressures. The sharp $(110)_T$ Bragg peaks of the tetragonal phase completely disappear in the high-pressure OR2 phase. The latter is characterized by 8 much broader $(101)_{OR2}$ type reflections, indicating significant sample degradation which is clearly due to the huge volume reduction and build-up of stress due to domains of the MnP-type structure with different orientations. We have observed

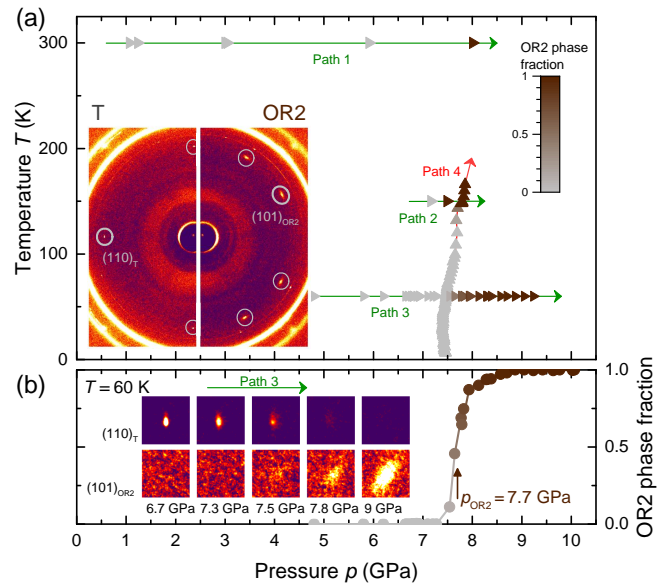


FIG. 8. The high-pressure structural transition of FeSe. (a) Points in the temperature-pressure phase diagram of FeSe with the fraction of the OR2 phase color-coded. The transition into the OR2 phase was observed to be abrupt and irreversible. The inset shows sections of the $(HK0)$ diffraction plane in the T and OR2 phases. The $(110)_T$ and $(101)_{OR2}$ and symmetry-equivalent reflections are highlighted by gray circles. (b) Phase fraction of the OR2 phase as evaluated by the relative intensity of the $(101)_{OR2}$ with respect to the $(110)_T$ Bragg reflections on increasing pressure at constant $T = 60$ K (path 3). The insets show the area surrounding these Bragg reflections at representative pressures.

this transition in measurements with increasing pressure at constant temperatures 60 K, 150 K and 300 K, in three different samples (from batch A) and also on temperature increase (concomitant with a slight pressure increase, see path 4 in the Fig. 8) in a sample from batch B. The fine pressure steps along path 3 allow to resolve particularly well the rapidly changing OR2 phase fraction between $p = 7.5 - 8.5$ GPa. Together, these four independent measurements define a sharp and nearly temperature-independent phase line at $p \approx 7.7$ GPa. We found this transition to have a severe hysteresis and to cause irreversible changes to the single-crystalline sample. For example, no return to the tetragonal phase was observed even after decreasing pressure down to 3 GPa and increasing temperature to 300 K following the measurement along path 2.

In previous reports using polycrystalline material^{37,38,50} and in a single-crystal study with glycerol pressure medium⁴², the structural transition into the OR2 phase has been observed at $p \sim 10 - 12$ GPa and often with a significant phase coexistence range. Our lower critical pressure is, however, close to the one reported in Refs. 51 and 69, which also used single crystals and He as pressure medium. This transition into a much more closely-packed crystal

structure at high pressures marks the end of the stability

of the layered structure of FeSe that shares its structural motive with iron-arsenide superconductors.

-
- * These authors contributed equally.
- ¹ P. Dai, *Rev. Mod. Phys.* **87**, 855 (2015).
 - ² A. Cano, M. Civelli, I. Eremin, and I. Paul, *Phys. Rev. B* **82**, 020408 (2010).
 - ³ A. Sapkota, G. S. Tucker, M. Ramazanoglu, W. Tian, N. Ni, R. J. Cava, R. J. McQueeney, A. I. Goldman, and A. Kreyssig, *Phys. Rev. B* **90**, 100504 (2014).
 - ⁴ C. de la Cruz, Q. Huang, J. W. Lynn, J. Li, W. R. II, J. L. Zarestky, H. A. Mook, G. F. Chen, J. L. Luo, N. L. Wang, and P. Dai, *Nature* **453**, 899 (2008).
 - ⁵ N. Ni, M. E. Tillman, J.-Q. Yan, A. Kracher, S. T. Hannahs, S. L. Bud'ko, and P. C. Canfield, *Phys. Rev. B* **78**, 214515 (2008).
 - ⁶ J.-H. Chu, J. G. Analytis, C. Kucharczyk, and I. R. Fisher, *Phys. Rev. B* **79**, 014506 (2009).
 - ⁷ R. M. Fernandes, A. V. Chubukov, and J. Schmalian, *Nature Physics* **10**, 97 (2014).
 - ⁸ R. M. Fernandes, L. H. VanBebber, S. Bhattacharya, P. Chandra, V. Keppens, D. Mandrus, M. A. McGuire, B. C. Sales, A. S. Sefat, and J. Schmalian, *Phys. Rev. Lett.* **105**, 157003 (2010).
 - ⁹ S. Nandi, M. G. Kim, A. Kreyssig, R. M. Fernandes, D. K. Pratt, A. Thaler, N. Ni, S. L. Bud'ko, P. C. Canfield, J. Schmalian, R. J. McQueeney, and A. I. Goldman, *Phys. Rev. Lett.* **104**, 057006 (2010).
 - ¹⁰ N. Ni, A. Thaler, J. Q. Yan, A. Kracher, E. Colombier, S. L. Bud'ko, P. C. Canfield, and S. T. Hannahs, *Phys. Rev. B* **82**, 024519 (2010).
 - ¹¹ D. R. Parker, M. J. P. Smith, T. Lancaster, A. J. Steele, I. Franke, P. J. Baker, F. L. Pratt, M. J. Pitcher, S. J. Blundell, and S. J. Clarke, *Phys. Rev. Lett.* **104**, 057007 (2010).
 - ¹² E. Hassinger, G. Gredat, F. Valade, S. R. de Cotret, A. Juneau-Fecteau, J.-P. Reid, H. Kim, M. A. Tanatar, R. Prozorov, B. Shen, H.-H. Wen, N. Doiron-Leyraud, and L. Taillefer, *Phys. Rev. B* **86**, 140502 (2012).
 - ¹³ S. Avci, O. Chmaissem, J. Allred, S. Rosenkranz, I. Eremin, A. Chubukov, D. Bugaris, D. Chung, M. Kanatzidis, J.-P. Castellan, J. Schlueter, H. Claus, D. Khalyavin, P. Manuel, A. Daoud-Aladine, and R. Osborn, *Nature Communications* **5**, 3845 (2014).
 - ¹⁴ A. E. Böhmer, F. Hardy, L. Wang, T. Wolf, P. Schweiss, and C. Meingast, *Nature Communications* **6**, 8911 (2015).
 - ¹⁵ J. M. Allred, K. M. Taddei, D. E. Bugaris, M. J. Krogstad, S. H. Lapidus, D. Y. Chung, H. Claus, M. Kanatzidis, D. E. Brown, J. Kang, R. M. Fernandes, I. Eremin, S. Rosenkranz, O. Chmaissem, and R. Osborn, *Nature Physics* **12** (2016).
 - ¹⁶ A. Kreyssig, M. G. Kim, S. Nandi, D. K. Pratt, W. Tian, J. L. Zarestky, N. Ni, A. Thaler, S. L. Bud'ko, P. C. Canfield, R. J. McQueeney, and A. I. Goldman, *Phys. Rev. B* **81**, 134512 (2010).
 - ¹⁷ J. M. Allred, S. Avci, D. Y. Chung, H. Claus, D. D. Khalyavin, P. Manuel, K. M. Taddei, M. G. Kanatzidis, S. Rosenkranz, R. Osborn, and O. Chmaissem, *Phys. Rev. B* **92**, 094515 (2015).
 - ¹⁸ E. Hassinger, G. Gredat, F. Valade, S. R. de Cotret, O. Cyr-Choinière, A. Juneau-Fecteau, J.-P. Reid, H. Kim, M. A. Tanatar, R. Prozorov, B. Shen, H.-H. Wen, N. Doiron-Leyraud, and L. Taillefer, *Phys. Rev. B* **93**, 144401 (2016).
 - ¹⁹ L. Wang, F. Hardy, T. Wolf, P. Adelman, R. Fromknecht, P. Schweiss, and C. Meingast, *physica status solidi (b)* **254**, 1600153 (2017).
 - ²⁰ K. M. Taddei, J. M. Allred, D. E. Bugaris, S. Lapidus, M. J. Krogstad, R. Stadel, H. Claus, D. Y. Chung, M. G. Kanatzidis, S. Rosenkranz, R. Osborn, and O. Chmaissem, *Phys. Rev. B* **93**, 134510 (2016).
 - ²¹ K. M. Taddei, J. M. Allred, D. E. Bugaris, S. H. Lapidus, M. J. Krogstad, H. Claus, D. Y. Chung, M. G. Kanatzidis, R. Osborn, S. Rosenkranz, and O. Chmaissem, *Phys. Rev. B* **95**, 064508 (2017).
 - ²² W. R. Meier, Q.-P. Ding, A. Kreyssig, S. L. Budko, A. Sapkota, K. Kothapalli, V. Borisov, R. Valentí, C. D. Batista, P. P. Orth, R. M. Fernandes, A. I. Goldman, Y. Furukawa, A. E. Böhmer, and P. C. Canfield, *npj Quantum Materials* **3**, 5 (2018).
 - ²³ T. M. McQueen, A. J. Williams, P. W. Stephens, J. Tao, Y. Zhu, V. Ksenofontov, F. Casper, C. Felser, and R. J. Cava, *Phys. Rev. Lett.* **103**, 057002 (2009).
 - ²⁴ M. D. Watson, T. K. Kim, A. A. Haghighirad, N. R. Davies, A. McCollam, A. Narayanan, S. F. Blake, Y. L. Chen, S. Ghannadzadeh, A. J. Schofield, M. Hoesch, C. Meingast, T. Wolf, and A. I. Coldea, *Phys. Rev. B* **91**, 155106 (2015).
 - ²⁵ Q. Wang, Y. Shen, B. Pan, Y. Hao, M. Ma, F. Zhou, P. Steffens, K. Schmalzl, T. R. Forrest, M. Abdel-Hafiez, X. Chen, D. A. Chareev, A. N. Vasiliev, P. Bourges, Y. Sidis, H. Cao, and J. Zhao, *Nature Materials* **15**, 159 (2016).
 - ²⁶ L. Fanfarillo, J. Mansart, P. Toulemonde, H. Cercellier, P. Le Fèvre, F. Bertran, B. Valenzuela, L. Benfatto, and V. Brouet, *Phys. Rev. B* **94**, 155138 (2016).
 - ²⁷ Y. Yamakawa, S. Onari, and H. Kontani, *Phys. Rev. X* **6**, 021032 (2016).
 - ²⁸ M. A. Tanatar, A. E. Böhmer, E. I. Timmons, M. Schütt, G. Drachuck, V. Taufour, K. Kothapalli, A. Kreyssig, S. L. Bud'ko, P. C. Canfield, R. M. Fernandes, and R. Prozorov, *Phys. Rev. Lett.* **117**, 127001 (2016).
 - ²⁹ M. Chinotti, A. Pal, L. Degiorgi, A. E. Böhmer, and P. C. Canfield, *Phys. Rev. B* **96**, 121112 (2017).
 - ³⁰ M. D. Watson, A. A. Haghighirad, L. C. Rhodes, M. Hoesch, and T. K. Kim, *New Journal of Physics* **19**, 103021 (2017).
 - ³¹ M. He, L. Wang, F. Hardy, L. Xu, T. Wolf, P. Adelman, and C. Meingast, *ArXiv e-prints* (2017), 1709.03861.
 - ³² A. E. Böhmer and A. Kreisel, *Journal of Physics: Condensed Matter* **30**, 023001 (2018).
 - ³³ M. Bendele, A. Amato, K. Conder, M. Elender, H. Keller, H.-H. Klauss, H. Luetkens, E. Pomjakushina, A. Raselli, and R. Khasanov, *Phys. Rev. Lett.* **104**, 087003 (2010).
 - ³⁴ Q. Wang, Y. Shen, B. Pan, X. Zhang, K. Ikeuchi, K. Iida, A. D. Christianson, H. C. Walker, D. T. Adroja, M. Abdel-Hafiez, X. Chen, D. A. Chareev, A. N. Vasiliev, and

- J. Zhao, *Nat. Comm.* **7**, 12182 (2016).
- ³⁵ F.-C. Hsu, J.-Y. Luo, K.-W. Yeh, T.-K. Chen, T.-W. Huang, P. M. Wu, Y.-C. Lee, Y.-L. Huang, Y.-Y. Chu, D.-C. Yan, and M.-K. Wu, *Proceedings of the National Academy of Sciences* **105**, 14262 (2008).
- ³⁶ Y. Mizuguchi, F. Tomioka, S. Tsuda, T. Yamaguchi, and Y. Takano, *Applied Physics Letters* **93**, 152505 (2008).
- ³⁷ S. Medvedev, T. M. McQueen, I. A. Troyan, T. Palasyuk, M. I. Erements, R. J. Cava, S. Naghavi, F. Casper, V. Ksenofontov, G. Wortmann, and C. Felser, *Nature Mat.* **8**, 630 (2009).
- ³⁸ S. Margadonna, Y. Takabayashi, Y. Ohishi, Y. Mizuguchi, Y. Takano, T. Kagayama, T. Nakagawa, M. Takata, and K. Prassides, *Phys. Rev. B* **80**, 064506 (2009).
- ³⁹ G. Garbarino, A. Sow, P. Lejay, A. Sulpice, P. Toulemonde, M. Mezouar, and M. Núñez-Regueiro, *EPL (Europhysics Letters)* **86**, 27001 (2009).
- ⁴⁰ J.-F. Ge, Z.-L. Liu, C. Liu, C.-L. Gao, D. Qian, Q.-K. Xue, Y. Liu, and J.-F. Jia, *Nature Materials* **14**, 285 (2015).
- ⁴¹ U. S. Kaluarachchi, V. Taufour, A. E. Böhmer, M. A. Tanatar, S. L. Bud'ko, V. G. Kogan, R. Prozorov, and P. C. Canfield, *Phys. Rev. B* **93**, 064503 (2016).
- ⁴² J. P. Sun, K. Matsuura, G. Z. Ye, Y. Mizukami, M. Shimosawa, K. Matsubayashi, M. Yamashita, T. Watashige, S. Kasahara, Y. Matsuda, J. Q. Yan, B. C. Sales, Y. Uwatoko, J. G. Cheng, and T. Shibauchi, *Nature Communications* **7**, 12146 (2016).
- ⁴³ K. Miyoshi, K. Morishita, E. Mutou, M. Kondo, O. Seida, K. Fujiwara, J. Takeuchi, and S. Nishigori, *Journal of the Physical Society of Japan* **83**, 013702 (2014).
- ⁴⁴ T. Terashima, N. Kikugawa, S. Kasahara, T. Watashige, T. Shibauchi, Y. Matsuda, T. Wolf, A. E. Böhmer, F. Hardy, C. Meingast, H. v. Löhneysen, and S. Uji, *Journal of the Physical Society of Japan* **84**, 063701 (2015).
- ⁴⁵ K. Kothapalli, A. E. Böhmer, W. T. Jayasekara, B. G. Ueland, P. Das, A. Sapkota, V. Taufour, Y. Xiao, E. E. Alp, S. L. Bud'ko, P. C. Canfield, A. Kreyssig, and A. I. Goldman, *Nature Communications* **7**, 12728 (2016).
- ⁴⁶ P. S. Wang, S. S. Sun, Y. Cui, W. H. Song, T. R. Li, R. Yu, H. Lei, and W. Yu, *Phys. Rev. Lett.* **117**, 237001 (2016).
- ⁴⁷ M. Bendele, A. Ichsanow, Y. Pashkevich, L. Keller, T. Strässle, A. Gusev, E. Pomjakushina, K. Conder, R. Khasanov, and H. Keller, *Phys. Rev. B* **85**, 064517 (2012).
- ⁴⁸ B. Büchner and C. Hess, *Nature Materials* **8**, 615 (2009).
- ⁴⁹ R. Khasanov, Z. Guguchia, A. Amato, E. Morenzoni, X. Dong, F. Zhou, and Z. Zhao, *Phys. Rev. B* **95**, 180504 (2017).
- ⁵⁰ R. S. Kumar, Y. Zhang, S. Sinogeikin, Y. Xiao, S. Kumar, P. Chow, A. L. Cornelius, and C. Chen, *The Journal of Physical Chemistry B* **114**, 12597 (2010).
- ⁵¹ V. Svitlyk, M. Raba, V. Dmitriev, P. Rodière, P. Toulemonde, D. Chernyshov, and M. Mezouar, *Phys. Rev. B* **96**, 014520 (2017).
- ⁵² A. E. Böhmer, V. Taufour, W. E. Straszheim, T. Wolf, and P. C. Canfield, *Phys. Rev. B* **94**, 024526 (2016).
- ⁵³ W. Bi, J. Zhao, J. Lin, Q. Jia, M. Y. Hu, C. Jin, R. Ferry, W. Yang, V. Struzhkin, and E. E. Alp, *Journal of Synchrotron Radiation* **22**, 760 (2015).
- ⁵⁴ W. Sturhahn, *Hyperfine Interact.* **125**, 149172 (2000).
- ⁵⁵ A. E. Böhmer, T. Arai, F. Hardy, T. Hattori, T. Iye, T. Wolf, H. v. Löhneysen, K. Ishida, and C. Meingast, *Phys. Rev. Lett.* **114**, 027001 (2015).
- ⁵⁶ C. Meingast, F. Hardy, R. Heid, P. Adelman, A. Böhmer, P. Burger, D. Ernst, R. Fromknecht, P. Schweiss, and T. Wolf, *Phys. Rev. Lett.* **108**, 177004 (2012).
- ⁵⁷ F. Hardy, T. Wolf, R. A. Fisher, R. Eder, P. Schweiss, P. Adelman, H. v. Löhneysen, and C. Meingast, *Phys. Rev. B* **81**, 060501 (2010).
- ⁵⁸ R. Prozorov, M. A. Tanatar, N. Ni, A. Kreyssig, S. Nandi, S. L. Bud'ko, A. I. Goldman, and P. C. Canfield, *Phys. Rev. B* **80**, 174517 (2009).
- ⁵⁹ S. Avci, O. Chmaissem, D. Y. Chung, S. Rosenkranz, E. A. Goremychkin, J. P. Castellán, I. S. Todorov, J. A. Schlueter, H. Claus, A. Daoud-Aladine, D. D. Khalyavin, M. G. Kanatzidis, and R. Osborn, *Phys. Rev. B* **85**, 184507 (2012).
- ⁶⁰ S. Avci, J. M. Allred, O. Chmaissem, D. Y. Chung, S. Rosenkranz, J. A. Schlueter, H. Claus, A. Daoud-Aladine, D. D. Khalyavin, P. Manuel, A. Llobet, M. R. Suchomel, M. G. Kanatzidis, and R. Osborn, *Phys. Rev. B* **88**, 094510 (2013).
- ⁶¹ V. Barzykin and L. P. Gor'kov, *Phys. Rev. B* **79**, 134510 (2009).
- ⁶² Y. Qi and C. Xu, *Phys. Rev. B* **80**, 094402 (2009).
- ⁶³ A. V. Chubukov, M. Khodas, and R. M. Fernandes, *Phys. Rev. X* **6**, 041045 (2016).
- ⁶⁴ R. Yu and Q. Si, *Phys. Rev. Lett.* **115**, 116401 (2015).
- ⁶⁵ J. K. Glasbrenner, I. I. Mazin, H. O. Jeschke, P. J. Hirschfeld, R. M. Fernandes, and R. Valentí, *Nature Physics* **11**, 953 (2015).
- ⁶⁶ D. D. Scherer, A. C. Jacko, C. Friedrich, E. Şaşıoğlu, S. Blügel, R. Valentí, and B. M. Andersen, *Phys. Rev. B* **95**, 094504 (2017).
- ⁶⁷ J. Ishizuka, T. Yamada, Y. Yanagi, and Y. Ōno, *Journal of the Physical Society of Japan* **87**, 014705 (2018).
- ⁶⁸ K. Y. Yip, Y. C. Chan, Q. Niu, K. Matsuura, Y. Mizukami, S. Kasahara, Y. Matsuda, T. Shibauchi, and S. K. Goh, *Phys. Rev. B* **96**, 020502 (2017).
- ⁶⁹ B. W. Lebert, V. Balédent, P. Toulemonde, J. M. Ablett, S. Klotz, T. Hansen, P. Rodière, M. Raba, and J.-P. Rueff, *ArXiv e-prints*, 1708.04805 (2017).